Experimental demonstration of dynamic temperature-dependent behaviour of UiO-66 metal-organic-framework: Compaction of hydroxylated and deydroxylated forms of UiO-66 for high pressure hydrogen storage

Sonwabo E. Bambalaza[a,b], Henrietta W. Langmi[c*], Robert Mokaya[d], Nicholas M. Musyoka[a*], Lindiwe E. Khotseng[b]

[a]*HySA Infrastructure Centre of Competence, Energy Centre, Council for Scientific and Industrial Research (CSIR), PO Box 395, Pretoria 0001, South Africa.*

[b]*Faculty of Natural Science, University of the Western Cape, Bellville, Cape Town 7535, South Africa.*

[c]*Department of Chemistry, University of Pretoria, Private Bag X20, Hatfield 0028, South Africa*

[d]*School of Chemistry, University of Nottingham, University Park, Nottingham, NG7 2RD, UK*

[*]Corresponding author 1: henrietta.langmi@up.ac.za Tel: +27 12 420 2800

[*]Corresponding author 2: nmusyoka@csir.co.za Tel: +27 12 841 4806

Abstract

High-pressure (700 MPa or ~100 000 psi) compaction of dehydroxylated and hydroxylated UiO-66 for H_2 storage applications is reported. The dehydroxylation reaction was found to occur between 150 – 300 ^oC. The H_2 uptake capacity of powdered hydroxylated UiO-66 reaches 4.6 wt% at 77 K and 100 bar, which is 21% higher than that of dehydroxylated UiO-66 (3.8 wt%). On compaction the H_2 uptake capacity of dehydroxylated UiO-66 pellets reduces by 66% from 3.8 wt% to 1.3 wt%, while for hydroxylated UiO-66 the pellets show only a 9% reduction in capacity from 4.6 wt% to 4.2 wt%. This implies the H_2 uptake capacity of compacted hydroxylated UiO-66 is at least three times higher than that of dehydroxylated UiO-66, and therefore hydroxylated UiO-66 is more promising for hydrogen storage applications. The H_2 uptake capacity is closely related to compaction induced changes in the porosity of UiO-66. The effect of compaction is greatest in partially dehydroxylated UiO-66 samples that are thermally treated at 200 and 290 ^oC. These compacted samples exhibit XRD patterns indicative of an amorphous material, low porosity (surface area reduces from between 700 and 1300 m^2/g to ca. 200 m^2/g and pore volume from between 0.4 and 0.6 cm^3/g to 0.1 and 0.15 cm^3/g) and very low hydrogen uptake (0.7 - 0.9 wt% at 77 K and 100 bar). The observed activation temperature-induced dynamic behaviour of UiO-66 is unusual for MOFs and has previously only been reported in computational studies. After compaction at 700 MPa, the structural properties and H_2 uptake of hydroxylated UiO-66 remain relatively unchanged, but are extremely compromised upon compaction of dehydroxylated UiO-66. Therefore, UiO-66 responds in a dynamic manner to changes in activation temperature within the range in which it has hitherto been considered stable.

Keywords: Hydrogen storage; UiO-66; dehydroxylation; hydroxylation; metal-organic framework; compaction

1. Introduction

Metal-organic frameworks have shown great promise in applications such as gas storage, gas separation, water treatment, catalysis, and as support materials in batteries [1–3]. The system integration of MOFs in application-specific technologies is envisaged on shaped MOF materials compared to MOFs in their pristine powder form [4–6]. The most common and successful shaping techniques used for shaping MOFs have been those that offer MOFs in the form of pellets [7], granules [8–10], membranes, or fibers [11]. There has, therefore, been interest in exploring the properties of MOFs in their shaped or fabricated forms. The shaping of MOFs is not only intended to improve the ease of handling MOF-based materials but may also play a role in enhancing some MOF material properties that are inherently diminished in the as-synthesized MOF powder form. For example, we have recently demonstrated a rare occasion where high pressure (~700 MPa) compaction of the zirconium-based MOF, UiO-66, into pellets drastically improves its volumetric H_2 storage capacity without compromising the gravimetric H_2 uptake [12]. Such property improvements on compaction may be attributed to the inherently high mechanical strength of the UiO-66 framework even in defective crystals. The property improvements were, however, reported for UiO-66 samples where the post-synthesis degassing/activation was carried out at 80 ^{o}C for 32 hours prior to all gas uptake measurements. It is, however, important to consider the fact that UiO-66 has been shown to exist in two stable forms, namely hydroxylated UiO-66 made up of $Zr_6O_4(OH)_4$ inorganic clusters and dehydroxylated UiO-66 that is

made up of Zr_6O_6 clusters [13]. The deydroxylation process occurs to completion at ca. 300 °C as follows [13,14]:

$$Zr_6O_4(OH)_2(s) \rightarrow Zr_6O_6(s) + 2H_2O(g) \quad \text{Eqn. (1)}$$

This transition may be virtually undetectable by PXRD analysis as shown in previous studies [14,15]. However in computational studies by Vandichel et al. [16,17], Rogge et al. [18] and others [19–21], dehydroxylation has been shown to have major implications on the mechanical stability of UiO-66.

The solvothermal synthesis of UiO-66 is commonly carried out in dimethylformamide (DMF) as the solvent due to the high solubility of terephthalic acid and zirconium chloride [22]. Upon completion of UiO-66 crystal growth, DMF molecules may remain trapped inside the UiO-66 pores, which necessitates post-synthesis evacuation. The most commonly used evacuation/activation methods include thermal treatment under vacuum at temperatures above the boiling point of DMF, or solvent exchange with a more volatile solvent such as ethanol or acetone [23,24]. It is therefore common practice for UiO-66 post-synthesis activation to be performed at 200 or 300 °C [25]. Using PXRD analysis, Valenzano and co-workers have shown that the structure of UiO-66 activated at these temperatures shows little change to crystalline phases and peak positions compared to the as-synthesised UiO-66 [14]. They found, however, a more detailed structure of the dehydroxylated UiO-66 compared to its hydroxylated form. Using extended X-ray absorption fine structure (EXAFS) analysis, Valenzano and co-workers showed that the crystalline structure of dehydroxylated UiO-66 (i.e., with Zr_6O_6 clusters) is more distorted compared to the hydroxylated UiO-66 form consisting of $Zr_6O_4(OH)_4$ inorganic clusters. Computational simulation studies by Vandichel et al. [16,17] and Hajek et al. [21] further predicted the possibility of bond rearrangements that may occur upon dehydroxylation of UiO-66. The computational

simulations of Vandichel et al [16,17] also detailed structural changes that may occur in UiO-66 during dehydroxylation processes up to 320 ^{o}C and proposed the possibility of two transition states involving bond rearrangements within the zirconium nodes. In addition, the study emphasized the role of defects on the extent of dehydroxylation, and that defects may result in significant compromising of the mechanical strength of the UiO-66 framework. The hydroxylated and dehydroxylated UiO-66 forms have further been shown to exhibit significant differences in their gas adsorption capacities for CO_2, CH_4, and H_2 [26,27], with dehydroxylated UiO-66 generally showing less adsorption capacity compared to hydroxylated UiO-66.

To our knowledge, there are hardly any experimental studies on the high-pressure compaction of dehydroxylated UiO-66, particularly as it relates to H_2 storage applications, and, furthermore, post-synthesis thermal treatment conditions vastly differ in previous reports [22,23,28,29]. In a sense, the importance of the thermal treatment (activation) temperature as it relates to material properties of UiO-66 has not always been given any consideration. In this regard, careful analysis of the effects of compaction of UiO-66 after post-synthesis thermal treatment (activation) in the temperature range of 80 to 320 ^{o}C, can provide valuable experimental information about the mechanical stability of hydroxylated and dehydroxylated UiO-66. This study, therefore, aimed to elucidate the effects of compaction not only on fully hydroxylated UiO-66 but also partially dehydroxylated and fully dehydroxylated UiO-66 samples and to propose optimum conditions for activation of UiO-66, towards hydrogen storage application.

2. Materials and methods

2.1. Chemicals

1,4-benzenedicarboxylic acid (BDC, Sigma Aldrich, 98 %), N,N-dimethylformamide (DMF, Sigma Aldrich, 99.8 %), zirconium (IV) tetrachloride ($ZrCl_4$, Sigma Aldrich, 99.5 %), formic acid (HCOOH, Sigma Aldrich, 95 %), and acetone (H_3COCH_3, Sigma Aldrich, 99.8 %). All the chemicals were purchased and used without further purification.

2.2. Preparation of UiO-66

The growth of UiO-66 crystallites was specifically done via an acid-modulated solvothermal method with formic acid (FA) as the monocarboxylic modulator. The synthesis method was adopted from our previous study [12] and typically involved sonicating a mixture containing 1:1:100 $ZrCl_4$:BDC:HCOOH in 300 mL DMF. The mixture was transferred to a round-bottom flask and maintained at 120 ^oC under reflux for 6 hours. After the synthesis, the white solid product was collected under centrifugation and washed in DMF for 3 hours. In order to remove DMF molecules possibly remaining within the pores, the product was further washed 3 times in acetone for 1 hour prior to recollection and drying under vacuum at room temperature for 24 hours.

2.3. Post-synthesis heat treatment and compaction

UiO-66 powder samples were heat-treated in a Micromeritics SmartVac at specified temperatures for 16 hours under vacuum (~10^{-7}). The temperatures of choice were as

follows: 80, 110, 140, 170, 200, 230, 260, 290, and 320^{o}C in order to obtain fully hydroxylated, partially dehydroxylated and fully dehydroxylated UiO-66 samples. For each of the heat-treated powder samples, a 400 mg portion was compacted at ~700 MPa using a Specac Manual Hydraulic Press and held at that pressure for 5 minutes.

2.4. Characterisation

To investigate the stability of the UiO-66 crystal structure, samples were analysed by powder X-ray diffraction (PXRD) whereby both powder and pellet samples were first ground into fine powder using an agate mortar and pestle. It is acceptable to grind the UiO-66 pellets after compaction since the uniaxial compaction of UiO-66 is an irreversible process [7,30–33]. The sample analysis was done on a Rigaku Ultima IV X-ray diffractometer with each measurement recorded from 2Θ angle of 3 to 90^{o} using 0.154 nm Ni-filtered Cu-K_{α} radiation (40 kV and 30 mA) at a scan rate of 2^{o} s^{-1}. The thermogravimetric (TG) plots for as-synthesised UiO-66 were obtained on a Mettler SDTA 851e TG analyser and a Discovery series Hi-res^{TM} TGA-MS for the compositional analysis of gaseous by-products given off during decomposition of UiO-66 in air and up to 1000 ^{o}C. The chemical composition of the UiO-66 structure remaining after heat treatment was analysed by Fourier transform infrared (FTIR) spectroscopy using a benchtop Bruker ALPHA II FTIR spectrometer from 4000 to 400 cm^{-1} at room temperature. Transmission electron microscopy (TEM) was used for imaging UiO-66 crystallite shapes and sizes obtained under the specified synthesis conditions. TEM imaging was carried out on a 200 kV JEOL-Jem 2100 model with samples first dispersed in methanol and ultrasonicated for 30 minutes prior to imaging. The Brunauer-Emmett-Teller (BET) surface areas and pore volumes were calculated from nitrogen (N_2) adsorption data measured on a Micromeritics 3-flex sorptometer

operating at 77 K. Excess hydrogen (H_2, 6.0 grade purity) uptake was measured at 77 K and 298 K up to 100 bar using a Hiden Isochema XEMIS intelligent gravimetric analyser. The H_2 uptake method was pre-set at specified time intervals between each measurement and the results obtained under non-equilibrium conditions. The H_2 uptake data, for each sample, was corrected for buoyancy effects using measured skeletal densities obtained from helium (He) pycnometry measurements at standard temperature and pressure (STP). The absolute or total H_2 uptake are calculated using Eqn. 2, taking into account H_2 adsorbed within the pores of the UiO-66. Calculation of volumetric H_2 capacity from gravimetric adsorption data has become somewhat controversial on whether the crystal density or packing density should be used to calculate volumetric H_2 capacities in MOFs [6,34–40]. Our previous study [12] was able to show strong correlation of the packing density to the volumetric H_2 capacity following the recommendations made in a publication by Balderas-Xicohténcatl et al. [35]. We, therefore, use the MOF packing density for both powder and compacted UiO-66 and calculate the volumetric H_2 capacity according to Eqn.3.

$$\theta_T = \theta_{Exc} + \frac{d_{H2}\, x\, V_T}{(1+d_{H2}\, x\, V_T)} x\ 100\% \qquad (2)$$

θ_T = total hydrogen uptake (wt%)

θ_{Exc} = excess hydrogen uptake (wt%)

d_{H2} = density ($g \cdot cm^{-3}$) of compressed H_2 gas at the relevant temperature and pressure. The H_2 densities at 77 K in the 0 - 100 bar range were obtained from the National Institute of Standards and Technology (NIST) website [41].

V_T = pore volume obtained from N_2 isotherm data.

$$v\theta_T = \theta_T\, x\, d_{MOF} \qquad (3)$$

$v\theta_T$= total volumetric uptake ($g \cdot L^{-1}$)

d_{MOF} = packing density of MOF material ($g \cdot L^{-1}$)

3. Results and Discussion

The morphology of the UiO-66 crystals obtained in this study show typical octahedral shapes consistent with what is reported in literature (ESI Fig. S1). The crystal structure of UiO-66 has been well studied [13,42,43] and has a cubic unit cell (F m – 3 m) with typical major peak positions at 2θ angles of ~ 8, 9, and 25° [14,44]. The PXRD pattern (ESI Fig. S1) shows intense peaks at the expected peak positions of 6, 8, and 25° and the diffraction pattern from 2θ ~3 to 90° matches most proposed CIF structures for UiO-66 synthesised under solvothermal conditions [14]. In particular, the two most intense peaks occur at 2θ angles of 7.4° and 8.5°, as shown in Fig. S1 (ESI), which shows synthesis of fully-formed UiO-66 phase instead of a possible polymorphic form, such as the Zr_6-based EHU-30 reported by Lee and co-workers [45]. In the case where the distinct UiO-66 peak positions are confirmed, the presence of the peak at 2θ ~ 6° typically suggests crystallites consisting of a symmetry forbidden phase (1 1 0) which has previously been attributed to a UiO-66 crystal with missing linker defects as reported by Shearer and co-workers [46]. The work of Liang et al. [47] also shows the use of formic acid modulator results in a UiO-66 structure with missing linker defects and their presence is indicated by a broad peak at 2θ ~ 6° in the measured UiO-66 XRD patterns. Indeed UiO-66 is known to be able to withstand a high level of tolerance towards structural defects without the crystal structure collapsing. Many studies have reported on stable UiO-66 defective structures with defect sites in the structure including missing terephthalate linkers or missing zirconia nodes [16,26,48–51]. Defective UiO-66 crystals have been generally obtained under acid-modulated and solvothermal crystal growth conditions similar to this study. In Fig. 1 the thermal decomposition of

UiO-66 was investigated by TG analysis, showing UiO-66 to be stable up to at least 500 °C, which is consistent with previous reports [14]. The remarkable thermal stability is attributed to the high connectivity of the Zr-O bonding in UiO-66 nodes which can be made up of $Zr_6O_4(OH)_4$ in the hydroxylated form or Zr_6O_6 in the dehydroxylated form [15,52,53]. The derivative weight (DTG) curves show the temperatures at which peak decomposition occurs. Three peaks observed at ~150, 250, and 500 °C for both the UiO-66 sample activated by solvent exchange with acetone and one degassed at 80 °C. Upon degassing at higher temperatures, i.e., 200 and 290 °C, the two peaks at 150 and 250 °C are no longer observable, indicating the removal of labile moieties or adsorbed molecules from the UiO-66 structure.

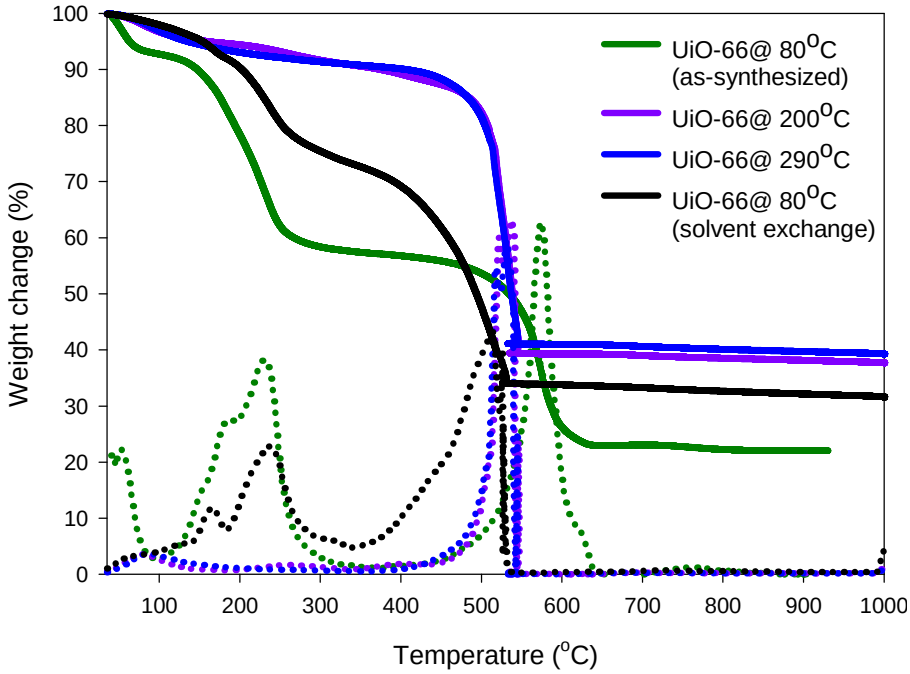

Figure 1: TGA curves showing the thermal decomposition of as-synthesised UiO-66 and after post-synthesis activation: degassed at 80 °C (black); degassed at 200 °C (purple); degassed at 290 °C (blue); solvent exchanged with acetone (yellow). Measured under 100 mL/h air flow at a heating (ramp) rate of 10 °C/min.

In Fig. 2, mass spectrometer (MS) signals were coupled to the TG curves in order to identify the composition of the gaseous by-products during the decomposition of UiO-66. The most prominent m/z signals showing peaks were m/z of 18, indicative of H_2O, and m/z of 44 typical for the presence of CO_2 [54,55]. The m/z 18 and m/z 44 signals both show a peak at ~150 and ~500 ^oC, with the m/z 18 signal showing a broad peak from ~150 to 300 ^oC and the m/z 44 signal a small peak at ~150 ^oC. The derivative weight loss (DTG) peaks observed up to 100 ^oC coincide with a large m/z 18 signal peak and indicate the presence of moisture. The thermal events observed above 100 ^oC may be considered as resulting from the decomposition of the UiO-66 structure or due to other contaminants other than moisture. From the comparison of FTIR spectra for as-synthesised UiO-66, DMF, and UiO-66 after acetone washing (Fig. 2(b)), it can be seen that a significant amount of DMF is part of the UiO-66 structure. The UiO-66 structure after solvent exchange with acetone shows very little evidence of vibrational bands at ~3000 cm^{-1}(–CH_3 stretch), ~1100 cm^{-1}(-CN stretch) and ~1700 cm^{-1}(C=O stretch), indicating the significant removal of DMF molecules [56]. The TG-MS profiles show that the m/z 44 signal can also indicate the presence of DMF molecules, which can be ionised in the MS chamber to generate resonance-stabilised $[N(CH_3)]^+$ ions due to the lone electron pairs of the nitrogen atom [57].

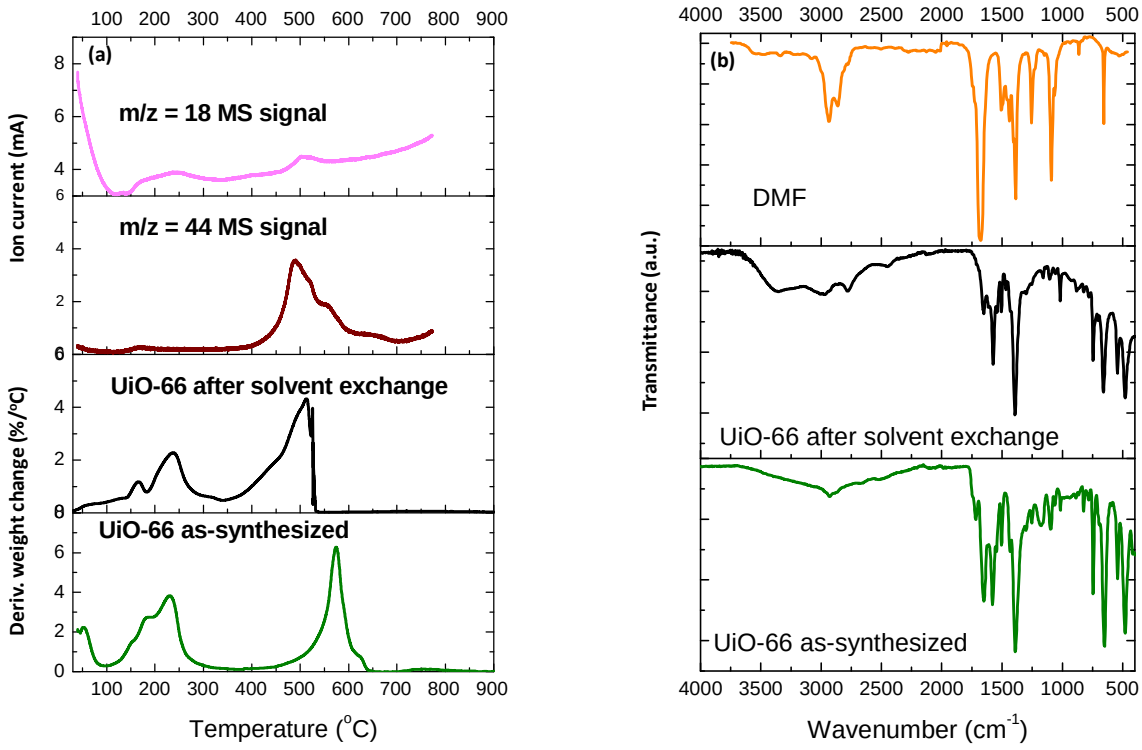

Figure 2: Thermal decomposition and chemical composition of UiO-66: (a) Overlay of derivative weight change (%/min) coupled to MS signals obtained during UiO-66 thermal decomposition under 100 mL/h air flow, and (b) FTIR spectra of DMF, as-synthesised UiO-66, and UiO-66 after solvent exchange with acetone.

The two most intense m/z signals for DMF are typically m/z 73 and m/z 44, which correspond to intact DMF molecules and $[N\text{-}(CH_3)_2]^+$ fragments respectively [55]. The absence of the m/z 73 signal may indicate sufficiently hot conditions in the MS combustion chamber that fragment DMF molecules. Indeed the m/z 44 signal is observable as a small peak at ca.150 - 200 °C and a larger peak at 400 – 700 °C. It is important to note that the m/z 44 signal is also very intense for CO_2^+, which result from the ionization of CO_2 molecules in the gaseous mixture [53]. The DMF molecules in UiO-66 are typically adsorbed solvent molecules within the pores of the as-synthesized UiO-66 crystallites, which are fully removed by degassing/activation at

200 – 300 ^{o}C under vacuum as shown in many studies [14,24,58,59]. The structure of UiO-66 is highly stable to heating, with decomposition at 450 – 500 ^{o}C, which corresponds to complete framework collapse [15,60,61.] The TG-MS profiles show that m/z 44 signal peaks at 150 – 200 ^{o}C represent the evacuation of adsorbed DMF molecules. The peak at 400 – 700 ^{o}C can be attributed to the evolution of CO_2(g) molecules resulting from the complete combustion of the terephthalate moieties from the UiO-66 framework given that the m/z 44 signal also coincides with the m/z 18 signal within the same temperature range. The complete combustion of any hydrocarbon material such as the terephthalate moieties in UiO-66 always leads to the production of CO_2(g) and H_2O(g) as final gaseous products [46]. The m/z 18 signal is also observed at lower temperatures, from 150 – 200 ^{o}C, and overlaps with the DMF peak signal (m/z 44). The evolution of water in this temperature range shows the dehydroxylation process of UiO-66 whereby $Zr_6O_4(OH)_2$ clusters are converted to Zr_6O_6 with the loss of two mol of H_2O [14]. This is a well-known and well-defined transition for UiO-66 [13,16,53], however, the fact that it overlaps with the evacuation of adsorbed DMF molecules may present problems in cases where a fully hydroxylated UiO-66 sample is required. Interestingly, in Fig. S4 (ESI), the TGA of solvent-exchanged UiO-66 obtained at different heating (ramp) rates of 3, 30, 50 and 100 ^{o}C/min under nitrogen (N_2) flow, show that there are indeed two distinct and consistent decomposition steps within the 150 – 300 ^{o}C temperature range. The two-step decomposition, represented by two peaks in the derivative weight curve, is observed to occur transiently between ~150 and 300 ^{o}C irrespective of the heating rate *and* the environmental conditions, since in Fig. 1 the two peaks are clearly observed in the thermal decomposition of solvent-exchanged UiO-66 under air flow. The results strongly indicates a transition state or intermediate UiO-66 structure during its dehydroxylation. The experimental results are consistent

with the results obtained in the computational studies conducted by Vandichel and co-workers [16,17], which predict the presence of transition states to occur during dehydroxylation of defective UiO-66. In their simulations, Vandichel and co-workers predict transient structural changes to occur via two steps, firstly the decoordination of terephthalate and hydroxyl groups from the $Zr_6O_4(OH)_4$ inorganic nodes; and the second step involves the extraction of a proton from bridging hydroxyl groups (μ_3-OH) by the free or dangling hydroxyl group, effectively recombining it into the $Zr_6O_4(OH)_4$ node. The study further shows that the two-step dehydroxylation process occurs in both defect-free and defective UiO-66, however, emphasizes that a high degree of defects enhances their proposed pathway during the process of dehydroxylation. The recent study by Hajek and co-workers [21], further proposes dynamic structural changes during dehydroxylation of UiO-66 as their simulation results show that during dehydroxylation/dehydration of UiO-66, the removal of hydroxyl groups from $Zr_6O_4(OH)_4$ nodes may trigger dynamic structural changes involving linker decoordination, hydrogen-bond stabilization of detached linker(s), and then recoordination of the linker(s).

In Fig. 3(a), the FTIR spectra of UiO-66 activated at 80, 200, 290, and 320 ^oC show a trend where two vibrational bands at ~700 and 550 cm^{-1} diminish as the activation temperature was increased from 80 to 320 ^oC. In compounds containing Zr-O bonding, the vibrational band at ~700 cm^{-1} is typically due to Zr-O stretch vibrations, which are expected in the UiO-66 inorganic nodes. A study by Valenzano et al. [14] reported the detailed structure of defect-free UiO-66 as consisting of $Zr_6O_4(OH)_4$ nodes coordinated to 12 terephthalate linkers, with each node having four bridging hydroxyl (–μOH-) groups and bridging oxo (μ-O-) groups giving rise to the typical Fm-3m UiO-66 crystal structure. The presence of defects, however, may cause

the inclusion of other molecules such as H_2O, monocarboxylates (e.g. formic acid), or other charge balancing molecules that may be present in the reaction mixture [48,59]. The possible presence of charge balancing molecules may contribute to extra phases in the UiO-66 crystal which would not be expected for a defect-free UiO-66 crystal lattice. Fig. 3(b) (and Fig. S2 ESI), show the PXRD patterns for UiO-66 powder samples activated by heating for 16 hours under vacuum at the specified temperatures. The main peaks at 2θ ~ 8, 9, and 25^o remain intact across all the activation temperatures indicating that the bulk structure of UiO-66 remains unchanged upon heating to 320 ^{o}C, a result also confirmed by TG data in Fig. 1. There are noticeable differences at some peak positions which may indicate changes to the crystal phases in the structure. At 170 ^{o}C and 200 ^{o}C, the peak at 2θ ~ 6^o and the two peaks between 9 and 12^o are not observed. At higher activation temperatures of 230 and 260 ^{o}C, the peak at 2θ ~ 6^o re-appears and the intensity of the peaks between 9 and 12^o remains significantly lower compared UiO-66 activated at 80 - 140 ^{o}C. The peak at 2θ ~ 6^o is not observed after activation at 290 ^{o}C and, furthermore, the peak at 2θ ~ 12^o is also not observed, but both peaks (at 2θ ~ 6 and 12^o) are observable after activation at 320 ^{o}C. The disappearance and reappearance of peaks observed in Fig. S2 may be an indication of transient or intermediate UiO-66 structure(s) following decoordination and protonation reactions during the dehydroxylation process pathway proposed by Vandichel et al. [16,17]. It is important to consider that the activation of the UiO-66 was not done in-situ, rather UiO-66 samples from the same batch were activated under vacuum at a specified temperature, i.e. one sample for each temperature. The possible structural effects of the observed differences in crystalline phases were investigated by analysing the gas sorption properties of UiO-66 following activation at the various temperatures. In order to exploit the properties of the fully

hydroxylated UiO-66, especially the high structural stability towards compaction [12,52,62], the temperature treatment of UiO-66 needs to be tailored to achieve a specific structure of UiO-66 (hydroxylated or dehydroxylated).

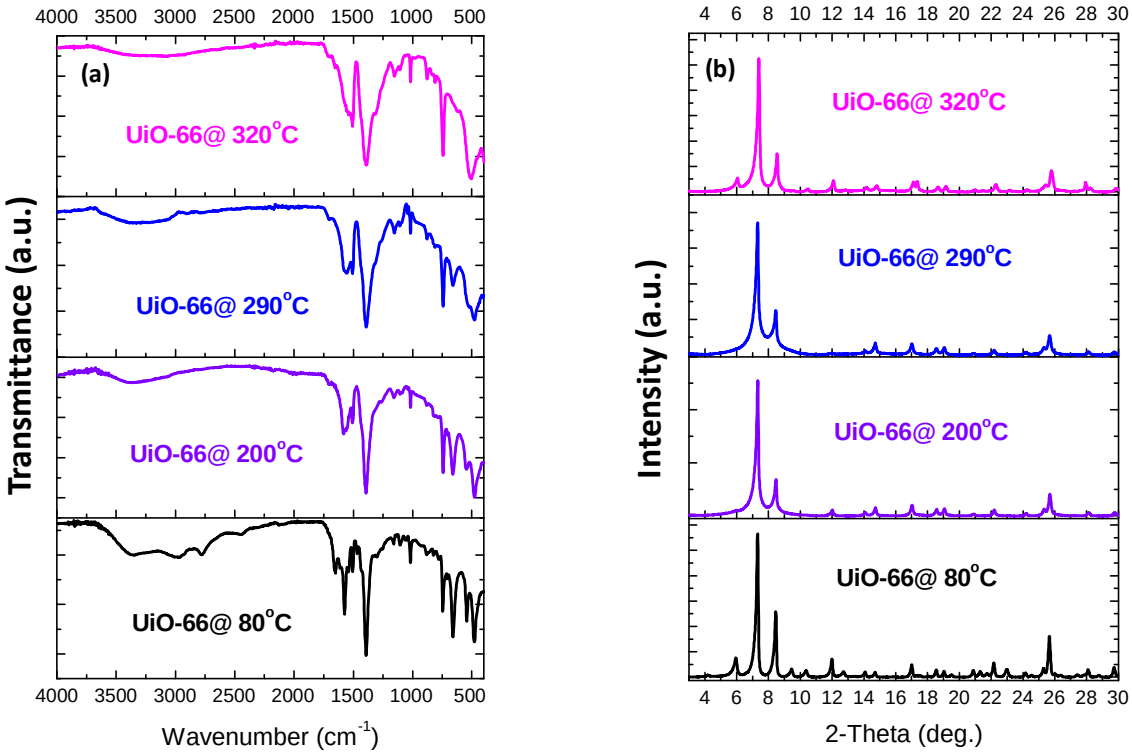

Figure 3: Chemical composition and structural analysis of UiO-66 after heat treatment at 80, 200, 290, and 320 °C: (a) FTIR spectra, and (b) PXRD patterns.

The nitrogen sorption isotherms in Fig. 4(a) indicate that there are significant activation temperature dependent changes in the porosity of UiO-66. The isotherms indicate that the porosity is greatest at activation temperature of 80 °C, and then decreases with activation temperature to a minimum at 290 °C, before again increasing at 320 °C. This indicates that the relationship between activation temperature and porosity is of a dynamic nature. The pore size distribution curves in Fig. 4(b) show that there are significant changes to the pore structure of UiO-66 with increasing activation temperatures. UiO-66 is a highly microporous MOF that almost

entirely possesses pore channels of size in the micropore range (2 to 20 Å). The pore channels of UiO-66 are typically of size ~6, 8, and 11 Å, which size relates to the free spaces in tetrahedral cages, triangular windows, and octahedral cages, respectively [14,63]. The major pore sizes shown in Fig. 4(b) are ~6, 7, 9, and 12 Å, which is consistent with reported literature [13,14,26]. The appearance of larger pore diameters above 12 Å may indicate the presence of open metal sites within a possibly defective UiO-66 structure. In the UiO-66 sample activated at 290 ^{o}C, the pore channels of size 6 Å, and above 12 Å are not observable, which is further indication of major structural changes to UiO-66. The evidence of possible structural changes can also be observed in variations in the surface area and pore volume (Table 1) wherein the order for powder samples is UiO-66$_{80^{o}C}$>UiO-66$_{200^{o}C}$> UiO-66$_{320^{o}C}$>UiO-66$_{290^{o}C}$. The higher porosity of UiO-66$_{320^{o}C}$ compared with UiO-66$_{290^{o}C}$ may be due to the suggested structural recombination, which is proposed by the work Vandichel et al. [16,17]. The trend not only indicates that low temperature activation/degassing at 80 ^{o}C (16 to 32 hours) was sufficient for removal of DMF solvent molecules from the pores of UiO-66, but also that dehydroxylation causes significant changes to the pore structure of UiO-66. It is, however, noteworthy that the proportion of micropore surface area maintained at ca. 90% and the micropore volume at ca. 80% (except for sample degassed at 290 ^{o}C, which had a lower value of ca. 65%). Bsed on the structural

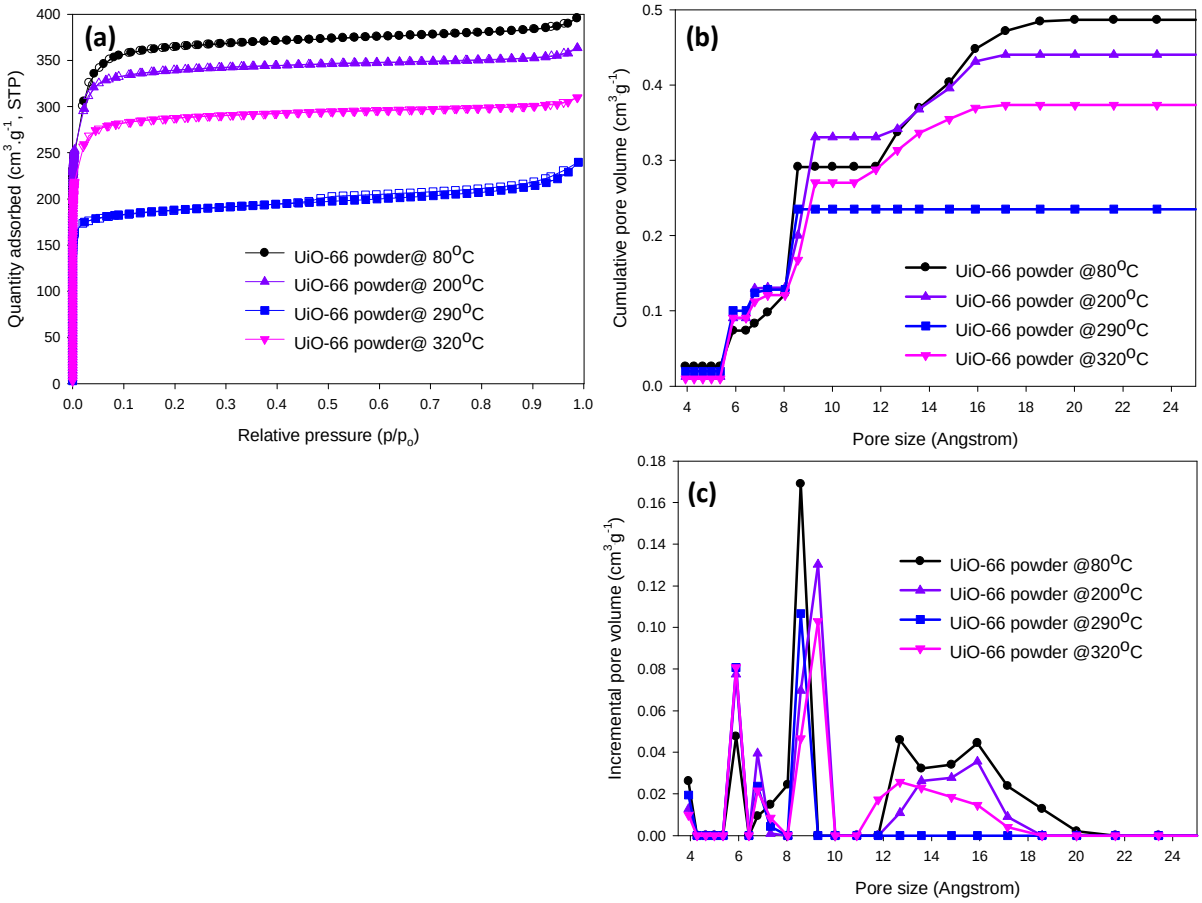

Figure 4: (a) Nitrogen adsorption/desorption isotherms at 77 K for UiO-66 activated at 80 (circle), 200 (triangle), 290 (square), and 320 °C (diamond). The open symbols represent desorption isotherms down to $p/p_o \approx 0.02$. (b) – (c) Cumulative and incremental NLDFT pore size distribution curves, in the micropore region, for UiO-66 activated at 80, 200, 290, and 320 °C. Isotherms representing repeat samples for UiO-66 activated at 290 and 320 °C are given in Figures S6 and S7, and corresponding textural properties in Table S1 (ESI).

Table 1: Textural properties of UiO-66 samples degassed at 80, 200, 290, or 320 ^{o}C before (powder) and after (pellet) compaction at 700 MPa.

Sample	Surface area[a] ($m^2 \cdot g^{-1}$)	Pore volume[b] ($cm^3 \cdot g^{-1}$)	Packing density ($g \cdot cm^{-3}$)	Volumetric surface area ($m^2 \cdot cm^{-3}$)[d]
UiO-66 powder@80^{o}C	1413 (1260, 89%)	0.61 (0.50, 82%)	0.65[c]	919
UiO-66 pellet@80^{o}C	1300 (1091, 84%)	0.60 (0.44, 73%)	1.52	1976
UiO-66 powder@200^{o}C	1307 (1194, 91%)	0.56 (0.48, 86%)	-	-
UiO-66 pellet@200^{o}C	252 (208, 83%)	0.15 (0.09, 60%)	1.33	335
UiO-66 powder@290^{o}C	708 (610, 86%)	0.37 (0.25, 68%)	-	-
UiO-66 pellet@290^{o}C	200 (163, 82%)	0.11 (0.07, 64%)	1.46	292
UiO-66 powder@320^{o}C	1100 (999, 91%)	0.48 (0.40, 83%)	-	-
UiO-66 pellet@320^{o}C	180 (123, 68%)	0.12 (0.05, 42%)	1.50	270

[a]Values in parenthesis are micropore surface area and percentage micropore surface area of the total surface area. [b]Values in parenthesis are micropore volume and percentage micropore of the total pore volume. [c]Tapped density of UiO-66 powder. [d]Calculated by multiplying the packing density and the surface area [35].

The H_2 adsorption isotherms, in Fig. 5, further substantiate the observed effects on the porosity. A similar trend is observable for both the excess H_2 uptake (Fig. S5, ESI) and the total/absolute H_2 uptake as shown in Fig. 5(a).The gas sorption results were obtained using volumetric (N_2) and gravimetric (H_2) techniques, which provides robust evidence of the observed post-synthesis thermal treatment induced behaviour of UiO-66. The surface area, pore volume, and total H_2 uptake of ~1400 $m^2.g^{-1}$, 0.6 $cm^3.g^{-1}$, and 4.6 wt% (at 77K and 100 bar), respectively, for UiO-66 powder activated at 80 ^{o}C are similar to results obtained in our previous study [12]. In Fig. 5(b), the H_2 uptake at 298 K was as expected lower compared to 77 K, and shows total uptake of ~0.8 wt% for hydroxylated UiO-66 (80 ^{o}C) and ~0.7 wt% for dehydroxylated UiO-66 (320 ^{o}C). It is typical for highly microporous materials to show near Type I gas adsorption isotherms at cryogenic temperatures, with fully Type I isotherms achievable

at the boiling point of the adsorbed gas [64], as shown in the N_2 adsorption isotherms in Fig. 4.

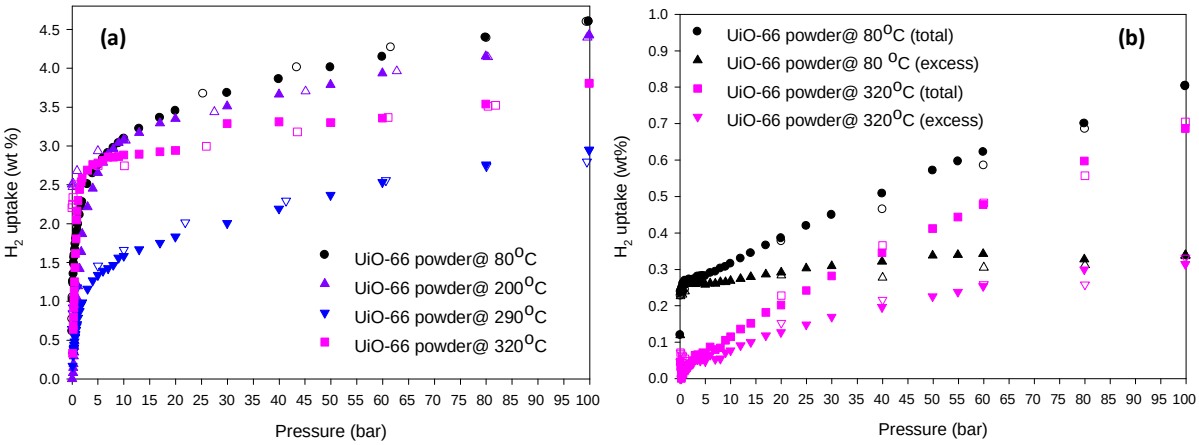

Figure 5: H_2 uptake isotherms for UiO-66 powder activated at 80, 200, 290, and 320 °C:(a) total/absolute gravimetric H_2 uptake at 77 K, and (b) total/absolute H_2 uptake at 298 K for UiO-66 powder activated at 80 and 320 °C. Open symbols represents desorption isotherms.

The effect of dehydroxylation on the mechanical stability, and hence gas adsorption properties, of UiO-66 was investigated by compacting the activated UiO-66 samples at ~700 MPa. In most cases of uniaxial compaction of MOFs, the surface area is compromised at increasing applied pressures [7,30–32,65] and to our knowledge, few attempts have been made to compact MOFs at a pressure of ~700 MPa. We have previously reported on the compaction of hydroxylated UiO-66 activated at 80 °C, and therefore in the current study the emphasis was on the possible differences in compacting dehydroxylated UiO-66, i.e. activated at 200, 290, and 320 °C. As shown in Fig. 6 and Table 1, similar porosity was observed for powdered and pelletized UiO-66 activated at 80 °C. The surface area of the UiO-66 pellet was 92% of that for the powder and 98% of pore volume was retained in the pellet. On the other hand, the

dehydroxylated UiO-66 (i.e., activated at 200 ^{o}C and above) show significantly reduced surface area, which reduced by more than 85% while the pore volume reduced by up to 80% for dehydroxylated UiO-66 pellet compared to hydroxylated UiO-66 powder. The reduction in porosity is a strong indication that the mechanical stability of UiO-66 is significantly reduced upon activation at 200, 290, and 320 ^{o}C compared to the high stability of UiO-66 activated at 80 ^{o}C. In addition to the work of Valenzano et al. [14], Chavan and co-workers [66] also demonstrated a "squeezing" of Zr_6O_6 clusters following the dehydroxylation of $Zr_6O_4(OH)_4$ clusters in hydroxylated UiO-66. Their work further demonstrated the effect in the isoreticular analogous Zr-MOF, UiO-67, and showed that the removal of –OH groups via dehydroxylation could result in a structural change that could slightly increase the Zr-Zr bond length and possibly compromise the mechanical stability of the Zr-MOF. The pore size distribution curves in Fig. 6(b) show that the pore channels of size 6 Å and above 12 Å are only observable in hydroxylated UiO-66 pellets and not in dehydroxylated UiO-66 pellets.

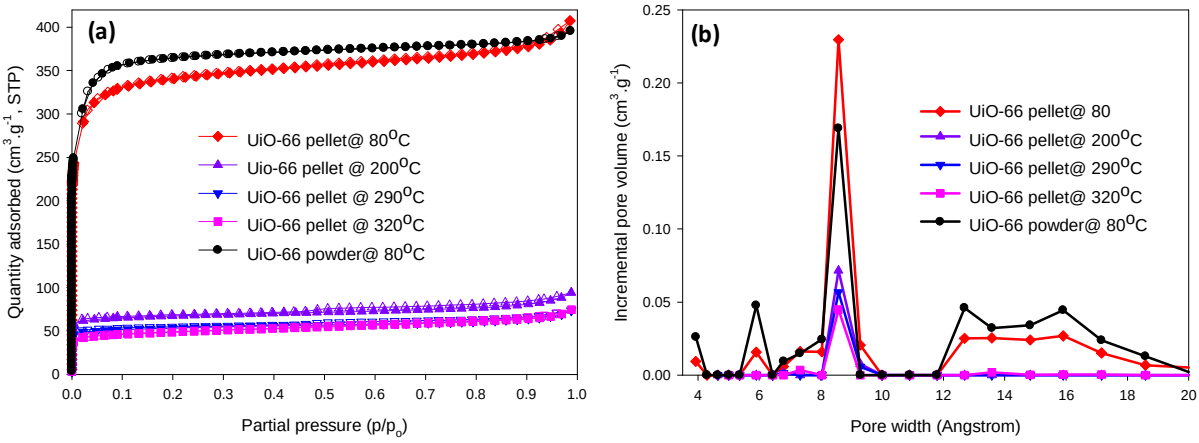

Figure 6: (a) N_2 sorption isotherms and pore size distribution curves for UiO-66 pellets activated at between 80 to 320 °C prior to compaction to pellets. (b) Pore size distribution curves obtained for UiO-66 pellets. Open symbols represent desorption isotherms.

There is also a drastic reduction in the total pore volume on compaction of UiO-66 activated at 200 to 320 °C. The PXRD patterns in Fig. S3 (ESI) show that the compaction of UiO-66 samples activated at temperatures above 170 °C have significant amorphous character compared to UiO-66 activated at lower temperatures. The peak positions, however, remain unchanged but major peak broadening is observable, especially for UiO-66 activated at 200 and 290 °C. The broadening of crystalline PXRD peaks generally represents possible amorphisation of crystallites and indeed the compaction of MOFs at sufficiently high pressures has been shown to result in partial or complete amorphisation [31]. The amorphisation process is particularly enhanced for MOFs with diminished or low mechanical strength (i.e., low bulk or shear modulus) [31,36,67–69]. The variations in porosity observed in this study strongly suggest possible reduction in the mechanical strength of dehydroxylated UiO-66 compared to hydroxylated UiO-66, which is a phenomena that has not previously been contemplated. Such differences in mechanical stability, which is one of the main

attractions of UiO-66, has major implications on the choice of post-synthesis treatment (i.e., activation temperature) of UiO-66 especially in applications where mechanical stability is essential. One such application is as hydrogen storage material where compaction or pelletization is essential.

As shown in Fig. 7 and summarised in Table 2, the hydroxylated UiO-66 pellet (activated at 80 ^{o}C) has a total H_2 uptake of 4.2 wt%, which is only 9% lower than that of the hydroxylated UiO-66 powder (4.6 wt%). The levels of hydrogen uptake are consistent with the porosity of the samples (Table 1). The relatively similar gravimetric hydrogen uptake means that the hydroxylated UiO-66 pellet has significantly higher volumetric H_2 capacity compared to the powder due to a rise in packing density occasioned by compaction. The results obtained for hydroxylated UiO-66 are consistent with our previous study [12]. The hydrogen uptake of dehydroxylated powder samples (200 – 320 ^{o}C) decreases compared to that of the hydroxylated sample in line with reductions in porosity, with the lowest uptake observed for the powder sample activated at 290 ^{o}C. Compaction of dehydroxylated UiO-66 results in drastic reduction in hydrogen uptake, with the reduction being greatest for samples compacted at 200 and 290 ^{o}C. The reduction in hydrogen uptake for the compacted dehydroxylated samples (Table 2) is in line with the changes in porosity (Table 1). We also determined the hydrogen storage working capacity, which is the difference in uptake at 100 bar compared to 1 bar. While hydroxylated samples (both powder and compacted) and powder forms of partially or fully dehydroxylated samples have working capacity of between 1.7 and 3.3 wt%, the results in Table 2 show much lower working capacity for compacted UiO-66 activated at 200 ^{o}C and above, especially for the compacted partially dehydroxylated UiO-66 samples activated at 200 and 290 ^{o}C. Indeed, the working capacity for these compacted partially dehydroxylated samples is almost nil

(ca. 0.2 wt%). It is noteworthy that the excess H_2 uptake isotherms in Fig. 7(b) show maximum excess capacity for hydroxylated UiO-66 powder at 30 bar, while in compacted hydroxylated and dehydroxylated UiO-66, the excess H_2 uptake maxima are shifted to ca. 50 bar and 100 bar, respectively. The observed shifting in excess H_2 adsorption maxima may be attributed to the densification of UiO-66 crystallites in the compacted forms. The close packing in compacted UiO-66 crystallites may result in grain boundary reductions, lowering the level of accessibility of H_2 to the UiO-66 pore structure. In addition, the H_2 uptake measurements were obtained under non-equilibrium conditions with pre-set equilibration times (20 minutes) for each measurement. As a result of kinetic effects, such as reduced mass transfer of H_2 into the pores of compacted UiO-66 [70], it is therefore possible to observe, at low pressures, low excess H_2 uptake in compacted UiO-66 compared UiO-66 powder.

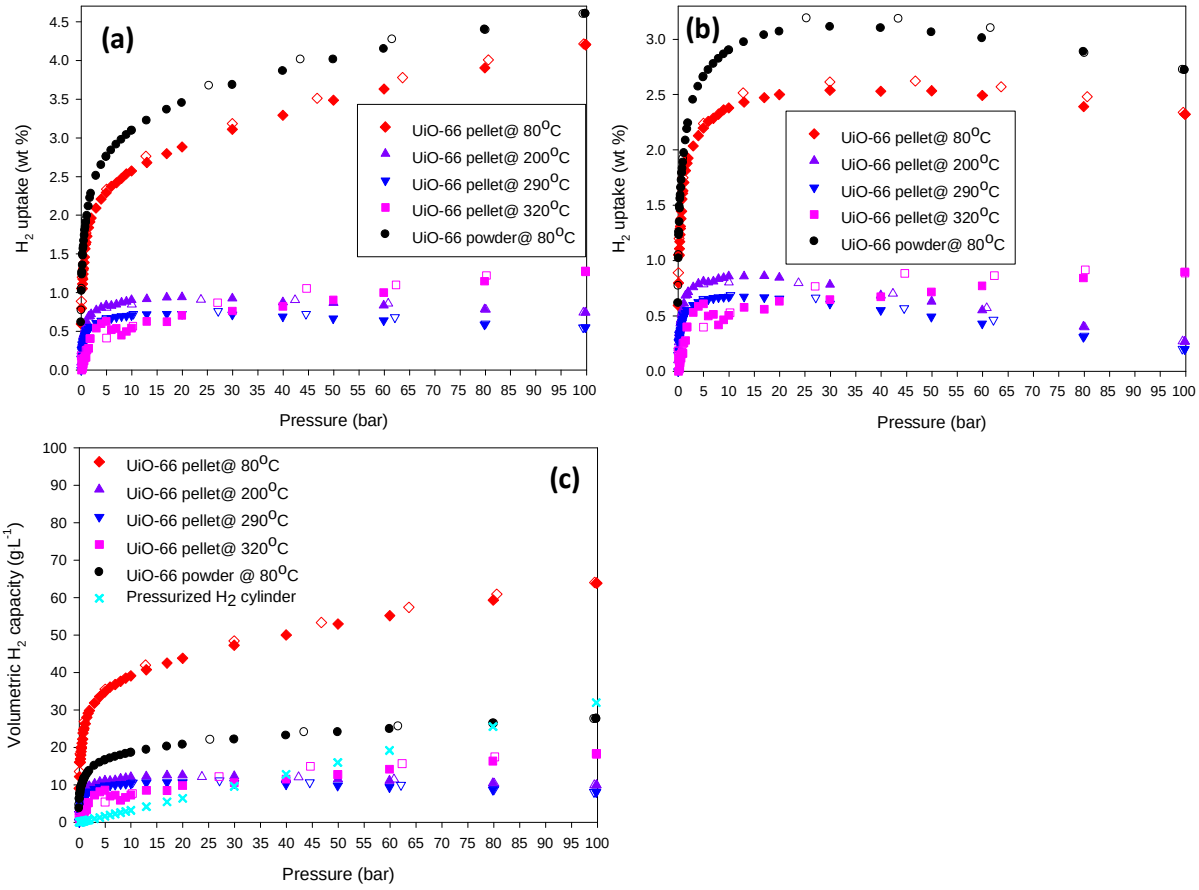

Figure 7: H_2 adsorption isotherms (77 K, 100 bar) for pelletized UiO-66 after activation at 80, 200, 290, and 320 °C: (a) total H_2 uptake, (b) excess H_2 uptake, (c) total volumetric H_2 capacity.

Table 2: Summary of the total gravimetric and volumetric H_2 uptake, at 77 K and up to 100 bar, for powdered and pelletized UiO-66 hydroxylated (activated at 80 ^oC) and dehydroxylated forms (after activation at 200, 290, and 320 ^oC).

Sample	Maximum excess H_2 uptake (wt%)[a]	Total gravimetric H_2 uptake (wt%)[b]		Working capacity (wt%)[c]	Total volumetric H_2 uptake at 100 bar ($g \cdot L^{-1}$)[c]	Working capacity ($g \cdot L^{-1}$)[d]
		1 bar	100 bar			
UiO-66 powder@80^{o}C	3.1 (2.8)	1.9	4.6	2.7	30	18
UiO-66 pellet@80^{o}C	2.5 (2.6)	1.7	4.2	2.5	64	38
UiO-66 powder@200^{o}C	3.0 (2.6)	1.1	4.4	3.3	-	-
UiO-66 pellet@200^{o}C	0.9 (0.5)	0.6	0.9	0.3	12	4
UiO-66 powder@290^{o}C	1.8 (1.4)	0.7	2.9	2.2	-	-
UiO-66 pellet@290^{o}C	0.7 (0.4)	0.5	0.7	0.2	10	3
UiO-66 powder@320^{o}C	2.8 (2.2)	2.1	3.8	1.7	-	-
UiO-66 pellet@320^{o}C	0.9 (0.4)	0.2	1.3	1.1	20	17
Pressurized H_2 cylinder						*30*

[a]Values in parenthesis are estimates from Chahine's Rule. [b]Calculated using eqn.2. [c]Calculated using eqn. 3. [d]Difference between the total H_2 uptake at 100 bar and 1 bar.

The volumetric H_2 capacity of hydroxylated UiO-66 increases significantly from 30 to 64 $g.L^{-1}$ after compaction, consistent with previous results [12]. Despite their increased packing density (Table 1), the compacted dehydroxylated samples activated at 200, 290, and 320 ^{o}C show much lower volumetric capacity (10–20 $g.L^{-1}$) compared to both powdered (30 $g.L^{-1}$) and compacted hydroxylated UiO-66 (64 $g.L^{-1}$). The low volumetric capacity of these dehydroxylated UiO-66 pellets samples is due to having significantly reduced volumetric surface areas as a consequence of their low porosity (surface area and pore volume) compared to their powdered counterparts (Figs. 4 and 6, and Table 1). In Fig. 7(c) and Table 2 the theoretical volumetric H_2

capacity of a pressurized cylinder is about 50 % of compacted UiO-66 (65 $g.L^{-1}$), and the working capacity of the latter is ca. 25% higher (38 $g.L^{-1}$ compared to 30 $g.L^{-1}$). Given that the volumetric working capacity of powder hydroxylated UiO-66 (18 $g.L^{-1}$) is lower than that of a pressurised cylinder, our result clearly shows the effect of compaction, and therefore mechanical stability, in improving the working capacity of MOFs as hydrogen storage materials. More importantly, our work clarifies on why it is important to understand the effects of post-synthesis treatment (such as activation temperature) on both the porosity and mechanical stability of MOFs especially those such as UiO-66 that are considered to be stable and unchanging over a wide temperature range. This work may also serve to show that UiO-66 responds in a dynamic manner to changes in activation temperature within the range in which it is considered stable. Furthermore, our findings can explain previously noted apparent inconsistencies in the porosity (and hydrogen storage capacity) of UiO-66 samples from a number of studies and labs. The past inconsistencies may, to some extent, be explained by differences in activation temperature, which has typically varied between 80 and 400 ^{o}C.

4. Conclusion

In this study, the post-synthesis heat treatment of UiO-66 up to 320 ^{o}C was monitored by TG-MS analysis and the results show a three-step decomposition process involving the removal of H_2O molecules via a two-step process between ~150 and 300 ^{o}C, termed dehydroxylation, and the third step involves framework collapse at ~500 ^{o}C. The TG-MS results also show the removal of DMF molecules at ~150 ^{o}C but FTIR results show that washing as-synthesized UiO-66 with acetone can sufficiently remove

DMF molecules without altering the UiO-66 structure *and* the three-step thermal decomposition of UiO-66 is maintained. In addition, TG results also showed that thermal decomposition of UiO-66 followed a three-step process even under inert conditions irrespective of heating (ramp) rates applied, which strongly suggests the dehydroxylation process to involve two UiO-66 transition states. The analysis of thermal decomposition in air shows that UiO-66 is stable up to ~500 ^{o}C, FTIR spectra reveal the removal of –OH groups from $Zr_6O_4(OH)_4$ nodes at 200, 290, and 320 ^{o}C, but PXRD patterns corresponding to those temperatures showed dynamic changes to some crystalline phases in response to high-temperature activation, which further provides evidence of dynamic temperature-dependent structural changes as proposed by Vandichel et al. [16,17]. Nitrogen sorption studies also confirm differences in the textural properties (surface area and pore volume) and pore structure of UiO-66 upon activation at 200, 290, and 320 ^{o}C. At these temperatures UiO-66 powder samples show reductions in surface areas of up to 30% compared to UiO-66 powder activated at 80 ^{o}C. There are drastic reductions of porosity for partially dehydroxylated UiO-66 (activated at 200 and 290 ^{o}C), after compaction at ~700 MPa, strongly indicating a compromise in the mechanical strength of UiO-66 at these temperatures. The computational studies on the high-pressure behaviour of UiO-66 with defects, reported by Vandichel et al. [17] and Rogge et al. [18], have previously proposed significant reductions in mechanical stability in UiO-66 with defects, which we, for the first time, experimentally evidence in this study. The work conducted by Vandichel et al. [16,17] also proposes the existence of transition states during the dehydroxylation process of UiO-66. In this study, the partially dehydroxylated UiO-66, activated at 200 and 290 ^{o}C, show very similar crystalline phases in the powder form and similarly show apparently high amorphous character, and almost nil hydrogen storage working

capacity (gravimetric and volumetric) after compaction at ~700 MPa. Interestingly, the PXRD patterns of dehydroxylated UiO-66 activated at 320 ^{o}C show peak positions that are similar to that of hydroxylated UiO-66, and also a higher hydrogen storage working capacity (at 77K, and 100 bar to 1 bar) for the compacted sample of 1.1 wt% (20 g.L^{-1} volumetric). The experimental results may, therefore, suggest that the mechanical stability of UiO-66 is possibly at its weakest at ~200 and ~290 ^{o}C followed by some degree of structure recombination post-dehydroxylation at 320 ^{o}C. This may also confirm the predicted dehydroxylation pathway proposed in the computational findings of Vandichel et al. [17] and Hajek et al. [21], whereby both defect-free and defective UiO-66 undergo decoordination, protonation, and recoordination reactions, which are enhanced in a highly defective UiO-66 crystal. Our results show total gravimetric H_2 uptake (at 77 K and 100 bar) for hydroxylated UiO-66 of 4.6 wt% (0.8 wt% at 298 K) for UiO-66 powder and 4.2 wt% for compacted UiO-66. The dehydroxylated UiO-66 activated at 320 ^{o}C shows total gravimetric H_2 uptake of 3.8 wt% (0.7 wt% at 298 K) for the powder and 1.3 wt% for compacted UiO-66. This shows only a 17% difference in the H_2 uptake between hydroxylated and dehydroxylated UiO-66 powders, but after compaction at ~700 MPa, the difference in H_2 uptake increases to ~70%. A similar trend is observable on the total volumetric H_2 capacities. The results obtained in this study give clear indication of the compromise in mechanical stability of UiO-66 in its dehydroxylated form and the resultant reduction in its textural properties and high-pressure H_2 uptake at 77 K and 298 K, which has implications for practical applications. It also clearly shows the effectiveness of solvent exchange prior to low-temperature activation (~80 ^{o}C), and how UiO-66 activation at 200 and 290 ^{o}C may generate UiO-66 structures with unexpectedly low mechanical stability. This study shows that the thermal decomposition of UiO-66 between 150 and 300 ^{o}C correspond

strongly to the predicted dehydroxylation pathway proposed by Vandichel et al. [17]. Based on TGA data, evidence of the presence of transition states during dehydroxylation was observable and dynamic changes to certain peak positions in the UiO-66 PXRD pattern may signify the dynamic structural changes (decoordination and protonation) predicted by Vandichel et al. [17]. It was also evident that the porosity, and hence gas adsorption properties, of UiO-66 is extremely sensitive to the high-temperature activation. Based on the results obtained in this study, we recommend that optimum post-synthesis treatment for UiO-66 should ideally include solvent exchange of the as-synthesised UiO-66 with volatile solvents (such as acetone or ethanol) followed by low-temperature activation not exceeding 150 ^{o}C. The proposed conditions should maintain the UiO-66 structure in its hydroxylated form, which is favourable for hydrogen storage applications.

Supplementary Information

Seven additional figures and one table, showing TEM images, XRD patterns, excess hydrogen uptake, and nitrogen isotherms and corresponding textural properties.

Acknowledgements

The authors would like to acknowledge financial support from the Royal Society – DFID Africa Capacity Building Initiative (ACBI) Programme (Grant No. AQ150029), and the South African Department of Science and Innovation (DSI) towards HySA Infrastructure (Project No. ENMH01X).

References

[1] Ardila-Suárez, C.; Perez-Beltran, S.; Ramírez-Caballero, G.; & Balbuena, P. Enhanced Acidity of Defective MOF-808: Effects of the Activation Process and Missing Linker Defects. Catal. Sci. Technol. 2018, 8(3), 847–857.

[2] Lyu, Q.; Deng, X.; Hu, S.; Lin, L.; & Ho, W. Exploring the Potential of Defective UiO-66 as Reverse Osmosis Membranes for Desalination. J. Phys. Chem. C 2019, 123(26), 16118–16126.

[3] Wales, D.; Grand, J.; Ting, V.; Burke, R.; Edler, K.; Bowen, C.; Mintova, S.; Burrows, A. Gas Sensing Using Porous Materials for Automotive Applications. Chem. Soc. Rev. 2015, 44(13), 4290–4321.

[4] Nandasiri, M.; Jambovane, S.; McGrail, B.; Schaef, H.; & Nune, S. Adsorption, Separation, and Catalytic Properties of Densified Metal-Organic Frameworks. Coord. Chem. Rev. 2016, 311, 38–52.

[5] Dailly, A.; & Poirier, E. Evaluation of an Industrial Pilot Scale Densified MOF-177 Adsorbent as an On-Board Hydrogen Storage Medium. Energy Environ. Sci. 2011, 4, 3527–3534..

[6] Purewal, J.; Liu, D.; Yang, J.; Sudik, A.; Siegel, D.; Maurer, S.; & Müller, U. (2012). Increased Volumetric Hydrogen Uptake of MOF-5 by Powder Densification. Int. J. Hydrogen Energy. 2012, 37, 2723–2727.

[7] Dhainaut, J.; Avci-Camur, C.; Troyano, J.; Legrand, A.; Canivet, J.; Imaz, I.; Maspoch, D.; Reinsch, H.; Farrusseng, D. Systematic Study of the Impact of MOF Densification into Tablets on Textural and Mechanical Properties. CrystEngComm 2017, 19(29), 4211–4218.

[8] Valekar, A.; Cho, K.; Lee, U.; Lee, J.; Yoon, J.; Hwang, Y.; Lee, S.; Cho, S.; Chang, J. Shaping of Porous Metal–Organic Framework Granules Using

Mesoporous ρ-Alumina as a Binder. RSC Adv. 2017, 7(88), 55767–55777.

[9] Iacomi, P.; Lee, U.; Valekar, A.; Chang, J.; & Llewellyn, P. Investigating the Effect of Alumina Shaping on the Sorption Properties of Promising Metal–Organic Frameworks. RSC Adv. 2019, 9(13), 7128–7135.

[10] Ren, J.; Musyoka, N.; Langmi, H.; Swartbooi, A.; North, B.; & Mathe, M. A more Efficient way to Shape Metal-Organic Framework (MOF) Powder Materials for Hydrogen Storage Applications. Int. J. Hydrogen Energy 2015, 40(13), 4617–4622.

[11] Wu, Y.; Li, F.; Liu, H.; Zhu, W.; Teng, M.; Jiang, Y.; Li, W.; Xu, D.; He, D.; Hannam, H.; Li, G. Electrospun Fibrous Mats as Skeletons to Produce Free-Standing MOF Membranes. J. Mater. Chem. 2012, 22(33), 16971.

[12] Bambalaza, S.; Langmi, H.; Mokaya, R.; Musyoka, N.; Ren, J.; & Khotseng, L. Compaction of a Zirconium Metal–Organic Framework (UiO-66) for High Density Hydrogen Storage Applications. J. Mater. Chem. A 2018, 6(46), 23569–23577.

[13] Chavan, S.; Vitillo, J.; Gianolio, D.; Zavorotynska, O.; Civalleri, B.; Jakobsen, S.; Nielsen, M.; Valenzano, L.; Lamberti, C.; Lillerud, K.; Bordiga, S. H2 Storage in Isostructural UiO-67 and UiO-66 MOFs. Phys. Chem. Chem. Phys. 2012, 14(5), 1614–1626.

[14] Valenzano, L.; Civalleri, B.; Chavan, S.; Bordiga, S.; Nilsen, M. H.; Jakobsen, S.; Lillerud, K.; Lamberti, C. Disclosing the Complex Structure of UiO-66 Metal Organic Framework: A Synergic Combination of Experiment and Theory. Chem. Mater. 2011, 23(7), 1700–1718.

[15] Cavka, J.; Jakobsen, S.; Olsbye, U.; Guillou, N.; Lamberti, C.; Bordiga, S.; Lillerud, K. A New Zirconium Inorganic Building Brick Forming Metal Organic

Frameworks with Exceptional Stability, J. Am. Chem. Soc. 2008, 130, 13850–13851.

[16] Vandichel, M.; Hajek, J.; Vermoortele, F.; Waroquier, M.; De Vos, D.E.; Van Speybroeck, V. Active Site Engineering in UiO-66 Type Metal–Organic Frameworks by Intentional Creation of Defects: A Theoretical Rationalization. CrystEngComm 2015, 17, 395–406.

[17] Vandichel, M.; Hajek, J.; Ghysels, A.; De Vos, A.; Waroquier, M.; & Van Speybroeck, V. Water Coordination and Dehydration Processes in Defective UiO-66 Type Metal Organic Frameworks. CrystEngComm 2016, 18(37), 7056–7069.

[18] Rogge, S.; Wieme, J.; Vanduyfhuys, L.; Vandenbrande, S.; Maurin, G.; Verstraelen, T.; Waroquier, M.; Van Speybroeck, V. Thermodynamic Insight in the High-Pressure Behavior of UiO-66: Effect of Linker Defects and Linker Expansion. Chem. Mater. 2016, 28(16), 5721–5732.

[19] Dissegna, S.; Vervoorts, P.; Hobday, C.; Düren, T.; Daisenberger, D.; Smith, A.; Fischer, R.; Kieslich, G. Tuning the Mechanical Response of Metal-Organic Frameworks by Defect Engineering. J. Am. Chem. Soc. 2018, 140, 11581−11584.

[20] Hajek, J.; Bueken, B.; Waroquier, M.; De Vos, D.; & Van Speybroeck, V. The Remarkable Amphoteric Nature of Defective UiO-66 in Catalytic Reactions. ChemCatChem 2017, 9(12), 2203–2210.

[21] Hajek, J.; Caratelli, C.; Demuynck, R.; De Wispelaere, K.; Vanduyfhuys, L.; Waroquier, M.; & Van Speybroeck, V. On the intrinsic dynamic nature of the rigid UiO-66 metal–organic framework. Chem. Sci. 2018, 9(10), 2723–2732.

[22] Zhao, Q.; Yuan, W.; Liang, J.; Li, J. Synthesis and Hydrogen Storage Studies

of Metal Organic Framework UiO-66, Int. J. Hydrogen Energy 2013, 38, 13104–13109.

[23] Ploskonka, A.; Marzen, S.; & DeCoste, J. Facile Synthesis and Direct Activation of Zirconium Based Metal–Organic Frameworks from Acetone. Ind. Eng. Chem. Res. 2017, 56(6), 1478–1484.

[24] Howarth, A.; Peters, A.; Vermeulen, N.; Wang, T.; Hupp, J.; & Farha, O. Best Practices for the Synthesis, Activation, and Characterization of Metal–Organic Frameworks. Chem. Mater. 2016, 29(1), 26–39.

[25] Liu, N.; Shi, L.; Meng, X. Tuning the Adsorption Properties of UiO-66 via Acetic Acid, J. Chem. Sci. 2019, 131, 1–7.

[26] Wu, H.; Chua, Y.; Krungleviciute, V.; Tyagi, M.; Chen, P.; Yildirim, T.; & Zhou, W. Unusual and Highly Tunable Missing-Linker Defects in Zirconium Metal–Organic Framework UiO-66 and Their Important Effects on Gas Adsorption. J. Am. Chem. Soc. 2013, 135(28), 10525–10532.

[27] Grissom, T.; Driscoll, D.; Troya, D.; Sapienza, N.; Usov, P.; Morris, A.; Morris, J. Molecular-Level Insight into CO2 Adsorption on the Zirconium- Based Metal − Organic Framework , UiO-66 : A Combined Spectroscopic and Computational Approach, J. Phys. Chem. C. 2019, 123, 13731–13738.

[28] Rasool, H.; Tian, H.; Ang, H.; Tade, M.; Buckley, C.; Wang, S. Nanosize Zr-Metal Organic Framework (UiO-66) for Hydrogen and Carbon Dioxide Storage, Chem. Eng. J. 2012, 187, 415–420.

[29] Moreira, M.; Dias, R.; Lee, U.; Chang, J.; Ribeiro, A.; Ferreira, A.; & Rodrigues, A. Adsorption Equilibrium of Carbon Dioxide, Methane, Nitrogen, Carbon Monoxide, and Hydrogen on UiO-66(Zr)_(COOH)2. J. Chem. Eng. Data 2019, 64(11), 4724-4732.

[30] Redfern, L.; Robison, L.; Wasson, M.; Goswami, S.; Lyu, J.; Islamoglu, T.; Chapman, K.; Farha, O. Porosity Dependence of Compression and Lattice Rigidity in Metal–Organic Framework Series, J. Am. Chem. Soc. 2019, 141, 4365–4371.

[31] Clearfield, A. Flexible MOFs Under Stress: Pressure and Temperature. Dalton Trans. 2016, 45(10), 4100–4112.

[32] Dhainaut, J.; Troyano, J.; Legrand, A.; Canivet, J.; Imaz, I.; Reinsch, H.; Farrusseng, D.; Dhainaut, J.; Troyano, J.; Legrand, A.; Canivet, J. Systematic Study of the Impact of MOF Densification Into Tablets on Textural and Mechanical Properties on Textural and Mechanical Properties. CrystEngComm, 2017,19, 4211-4218

[33] Raj, M.; Senthilkumar, S.; Somani, R.; Bajaj, H. Preparation, Characterization and Hydrogen Sorption Study of MIL-101(Cr) pellets, Int. J. Environ. Stud. 2016, 73, 357–368.

[34] Ahmed, A.; Liu, Y.; Purewal, J.; Tran, L.; Wong-Foy, A.; Veenstra, M.; Matzger, A.; Siegel, D. Balancing Gravimetric and Volumetric Hydrogen Density in MOFs, Energy Environ. Sci. 2017, 10, 2459–2471.

[35] Balderas-Xicohténcatl, R.; Schlichtenmayer, M.; Hirscher, M. Volumetric Hydrogen Storage Capacity in Metal-Organic Frameworks, Energy Technol. 2017, 6(3), 578–582.

[36] Ardelean, O.; Blanita, G.; Borodi, G.; Lazar, M.D.; Misan, I.; Coldea, I.; Lupu, D. Volumetric hydrogen adsorption capacity of densified MIL-101 monoliths, Int. J. Hydrogen Energy. 2013, 38, 7046–7055.

[37] Parilla, P.; Gross, K.; Hurst, K.; Gennett, T. Recommended Volumetric Capacity Definitions and Protocols for Accurate, Standardized and

Unambiguous Metrics for Hydrogen Storage Materials, Appl. Phys. A Mater. Sci. Process. 2016, 122, 1–18.

[38] Yan, Y.; Silva, I.; Blake, A.J.; Dailly, A.; Manuel, P.; Yang, S.; Der, M.S. High Volumetric Hydrogen Adsorption in a Porous Anthracene- Decorated Metal − Organic Framework, Inorg. Chem. 2018, 57, 19, 12050-12055.

[39] Zacharia, R.; Cossement, D.; Lafi, L.; Chahine, R. Volumetric Hydrogen Sorption Capacity of Monoliths Prepared by Mechanical Densification of MOF-177, J. Mater. Chem. 2010, 20, 2145–2151.

[40] Yang, J.; Sudik, A.; Wolverton, C.; Siegel, D. High Capacity Hydrogenstorage Materials: Attributes for Automotive Applications and Techniques for Materials Discovery, Chem. Soc. Rev. 2010, 39, 656–675.

[41] Physical Properties of Fluid Systems, Cited online, 12 September 2019, from: https://webbook.nist.gov/chemistry/fluid/.

[42] Platero-Prats, A.; Mavrandonakis, A.; Gallington, L.; Liu, Y.; Hupp, J.; Farha, O.; Cramer, C.; Chapman, K. Structural Transitions of the Metal-Oxide Nodes within Metal–Organic Frameworks: On the Local Structures of NU-1000 and UiO-66. J. Am. Chem. Soc. 2016, 138(12), 4178–4185.

[43] Katz, M.; Brown, Z.; Colón, Y.; Siu, P.; Scheidt, K.; Snurr, R.; Hupp, J.; Farha, O. A Facile Synthesis of UiO-66, UiO-67 and Their Derivatives. ChemComm 2013, 49(82), 9449.

[44] Shearer, G., Chavan, S., Bordiga, S., Svelle, S., Olsbye, U., & Lillerud, K. Defect Engineering: Tuning the Porosity and Composition of the Metal–Organic Framework UiO-66 via Modulated Synthesis. Chem. Mater. 2016, 28(11), 3749–3761.

[45] Lee, S.; Mancuso, J.; Le, K.; Malliakas, C.; Bae, Y.; Hendon, C.; Islamoglu, T.;

Farha, O. Time-Resolved in Situ Polymorphic Transformation from One 12-Connected Zr-MOF to Another. ACS Materials Lett. 2020, 2(5), 499–504.

[46] Shearer, G.; Chavan, S.; Ethiraj, J.; Vitillo, J.; Svelle, S.; Olsbye, U.; Lamberti, C.; Bordiga, S.; Lillerud, K. Tuned to perfection: Ironing Out the Defects in Metal-Organic Framework UiO-66, Chem. Mater. 2014, 26, 4068–4071.

[47] Liang, W.; Coghlan, C.; Ragon, F.; Rubio-Martinez, M.; D'Alessandro, D.; & Babarao, R. Defect Engineering of UiO-66 for CO2 and H2O Uptake – a Combined Experimental and Simulation Study. Dalton Trans. 2016, 45(11), 4496–4500.

[48] Shearer, G.; Chavan, S.; Bordiga, S.; Svelle, S.; Olsbye, U.; Lillerud, K. Defect Engineering: Tuning the Porosity and Composition of the Metal-Organic Framework UiO-66 via Modulated Synthesis, Chem. Mater. 2016, 28, 3749–3761.

[49] Chong, S.; Thiele, G., & Kim, J. Excavating Hidden Adsorption Sites in Metal-Organic Frameworks Using Rational Defect Engineering. Nat. Commun. 2017, 8(1).

[50] Liu, L.; Chen, Z.; Wang, J.; Zhang, D.; Zhu, Y.; Ling, S.; Huang, K.; Belmabkhout, Y.; Adil, K.; Zhang, Y.; Slater, B.; Eddaoudi, M.; Han, Y. Imaging Defects and Their Evolution in A Metal–Organic Framework at Sub-Unit-Cell Resolution, Nat. Chem. 2019, 11, 622–628.

[51] Cliffe, M.; Wan, W.; Zou, X.; Chater, P.; Kleppe, A.; Tucker, M.; Wilhelm, H.; Funnell, N.; Coudert, F.; & Goodwin, A. Correlated Defect Nanoregions in a Metal–Organic Framework. Nat. Commun. 2014, 5(1).

[52] Wu, H.; Yildirim, T.; & Zhou, W. Exceptional Mechanical Stability of Highly Porous Zirconium Metal–Organic Framework UiO-66 and Its Important

Implications. J. Phys. Chem. Lett 2013, 4(6), 925–930.

[53] Canivet, J.; Vandichel, M.; & Farrusseng, D. Origin of Highly Active Metal–Organic Framework Catalysts: Defects? Defects! Dalton Trans. 2016, 45(10), 4090–4099.

[54] Mass spectrum of water, Cited online, 20 September 2019, from: https://webbook.nist.gov/cgi/inchi?ID=C7732185&Mask=200.

[55] Mass spectrum of carbon dioxide, Cited online, 20 September 2019, from: https://webbook.nist.gov/cgi/inchi?ID=C124389&Mask=200.

[56] Infrared spectrum of dimethylformamide, Cited online, 12 September 2019, from: https://webbook.nist.gov/cgi/cbook.cgi?ID=C68122&Units=SI&Type=IR-SPEC&Index=2#IR-SPEC.

[57] Mass spectrometer of dimethylformamide, Cited online, 20 September 2019, from: https://webbook.nist.gov/cgi/cbook.cgi?ID=C68122&Units=SI&Mask=200#Mass-Spec.

[58] Kandiah, M., Nilsen, M., Usseglio, S., Jakobsen, S., Olsbye, U., Tilset, M., Larabi, C.; Quadrelli, E.; Bonino, F.; Lillerud, K. Synthesis and Stability of Tagged UiO-66 Zr-MOFs. Chem. Mater. 2010, 22(24), 6632–6640.

[59] Schaate, A.; Roy, P.; Godt, A.; Lippke, J.; Waltz, F.; Wiebcke, M.; Behrens, P. Modulated Synthesis of Zr-Based Metal-Organic Frameworks: From Nano to Single Crystals, Chem. - A Eur. J. 2011, 17, 6643–6651.

[60] Ren, J.; Segakweng, T.; Langmi, H.; Musyoka, N.; North, B.; Mathe, M.; Bessarabov, D. Microwave-Assisted Modulated Synthesis Of Zirconium-Based Metal-Organic Framework (Zr-MOF) for Hydrogen Storage Applications, Int. J. Mater. Res. 2014, 105, 516–519.

[61] Ren, J.; Langmi, H.; North, B.; Mathe, M.; Bessarabov, D. Modulated Synthesis Of Zirconium-Metal Organic Framework (Zr-MOF) for Hydrogen Storage Applications, Int. J. Hydrogen Energy. 2014, 39, 890–895.

[62] Peterson, G.; Decoste, J.; Glover, T.; Huang, Y.; Jasuja, H.; Walton, K. Effects of Pelletization Pressure on the Physical And Chemical Properties of the Metal-Organic Frameworks Cu3(BTC)2 and UiO-66, Microporous Mesoporous Mater. 2013, 179, 48–53.

[63] Katz, M.; Brown, Z.; Colón, Y.; Siu, P.; Scheidt, K.; Snurr, R.; Hupp, J.; Farha, O. A Facile Synthesis of UiO-66, UiO-67 and Their Derivatives, Chem. Commun. 2013, 49, 9449.

[64] Thommes, M.; Kaneko, K.; Neimark, A.; Olivier, J.; Rodriguez-Reinoso, F.; Rouquerol, J.; Sing, K. Physisorption of Gases, With Special Reference to the Evaluation of Surface Area and Pore Size Distribution (IUPAC Technical Report), Pure Appl. Chem. 2015, 87, 1051–1069.

[65] Rogge, S.; Waroquier, M.; & Van Speybroeck, V. Reliably Modeling the Mechanical Stability of Rigid and Flexible Metal–Organic Frameworks. Acc. Chem. Res. 2017, 51(1), 138–148.

[66] Chavan, S.; Vitillo, J.; Gianolio, D.; Zavorotynska, O.; Civalleri, B.; Jakobsen, S.; Nilsen, M.; Valenzano, L.; Lamberti, C.; Lillerud, K.; Bordiga, S. H2 Storage in Isostructural UiO-67 and UiO-66 MOFs, Phys. Chem. Chem. Phys. 2012, 14, 1614–1626.

[67] Chapman, K.; Halder, G.; Chupas, P. Induced Amorphization and Porosity Modification in a Metal− Organic Framework, J. Am. Chem. Soc. 2009, 131, 17546–17547.

[68] Blanita, G.; Coldea, I.; Misan, I.; Lupu, D. Hydrogen cryo-adsorption by

hexagonal prism monoliths of MIL-101, Int. J. Hydrogen Energy. 2014, 39, 17040–17046.

[69] Coudert, F. Responsive Metal-Organic Frameworks and Framework Materials: Under Pressure, Taking The Heat, in the Spotlight, with Friends, Chem. Mater. 2015, 27, 1905–1916.

[70] Xu, C.; Yang, J.; Veenstra, M.; Sudik, A.; Purewal, J.; Ming, Y.; Hardy, B.; Warner, J.; Maurer, S.; Mu, U.; Siegel, D. Hydrogen permeation and diffusion in densified MOF-5 pellets, Int. J. Hydrog. Energy 2013, 38(8), 3268–3274.

Table of Contents (TOC) graphic